

Channelization cascade in landscape evolution

*Original*

Channelization cascade in landscape evolution / Bonetti, Sara; Hooshyar, Milad; Camporeale, Carlo; Porporato, Amilcare. - In: PROCEEDINGS OF THE NATIONAL ACADEMY OF SCIENCES OF THE UNITED STATES OF AMERICA. - ISSN 0027-8424. - STAMPA. - (2020), p. 201911817. [10.1073/pnas.1911817117]

*Availability:*

This version is available at: 11583/2779296 since: 2020-01-11T14:49:20Z

*Publisher:*

National Academy of Science

*Published*

DOI:10.1073/pnas.1911817117

*Terms of use:*

This article is made available under terms and conditions as specified in the corresponding bibliographic description in the repository

*Publisher copyright*

(Article begins on next page)

# Landscape channelization cascade

Sara Bonetti<sup>a</sup>, Milad Hooshyar<sup>b,c</sup>, Carlo Camporeale<sup>d</sup>, and Amilcare Porporato<sup>b,c,1</sup>

<sup>a</sup>Department of Environmental Systems Science, ETH Zurich, 8092 Zurich, Switzerland; <sup>b</sup>Department of Civil and Environmental Engineering, Princeton University, Princeton, New Jersey 08544, USA; <sup>c</sup>Princeton Environmental Institute, Princeton university, Princeton, New Jersey 08544, USA; <sup>d</sup>Department of Environment, Land and Infrastructure Engineering, Politecnico di Torino, 10129 Turin, Italy

This manuscript was compiled on December 1, 2019

1 **The hierarchy of channel networks in landscapes displays features**  
2 **that are characteristic of non-equilibrium complex systems. Here we**  
3 **show that a sequence of increasingly complex ridge and valley net-**  
4 **works is produced by a system of partial differential equations cou-**  
5 **pling landscape evolution dynamics with a specific catchment area**  
6 **equation. By means of a linear stability analysis we identify the cri-**  
7 **tical conditions triggering channel formation and the emergence of**  
8 **characteristic valley spacing. The ensuing channelization cascade,**  
9 **described by a dimensionless number accounting for diffusive soil**  
10 **creep, runoff erosion, and tectonic uplift, is reminiscent of the sub-**  
11 **sequent instabilities in fluid turbulence, while the structure of the**  
12 **simulated patterns is indicative of a tendency to evolve toward op-**  
13 **timal configurations, with anomalies similar to dislocation defects**  
14 **observed in pattern-forming systems. The choice of specific geomor-**  
15 **phic transport laws and boundary conditions strongly influences the**  
16 **channelization cascade, underlying the nonlocal and nonlinear char-**  
17 **acter of its dynamics.**

Ridge and valley patterns | Landscape evolution model | Detachment limited | River networks | Drainage area

1 **T**he spatial distribution of ridges and valleys, including the  
2 formation of evenly spaced first order valleys as well as  
3 more complex branching river networks (see Fig. 1), is one of  
4 the most striking features of a landscape. It has long fascinated  
5 the scientific community, leading to the development of a rich  
6 body of work on the statistical, theoretical, and numerical  
7 analysis of landscape organization. Early works focused on  
8 the definition of stream ordering systems for the river basin  
9 characterization (1–3) and the coupled dynamics of water and  
10 sediment transport to identify stability conditions for incipient  
11 valley formation (4–6), followed by the statistical description  
12 of river networks, including scaling laws and fractal properties  
13 of river basins (7–10), the related optimality principles (9, 11),  
14 and stochastic models (12–14). These studies have shed light  
15 on the spatial organization and governing statistical laws of  
16 developed river networks and explored the linkages to other  
17 branch-forming systems (13, 15, 16), but have not tackled the  
18 physical origin of the underlying instabilities and feedback  
19 mechanisms acting over time in the formation of the observed  
20 ridge and valley patterns (17). To this purpose, landscape evo-  
21 lution models have been employed for the analysis of branching  
22 river networks (18, 19) in relation to the main erosional mech-  
23 anisms acting on the topography. These works represented  
24 an important step forward in the study of spatially organized  
25 patterns of ridges and valleys. However, lacking a rigorous  
26 formulation of the drainage area equation (20, 21) precluded  
27 the theoretical investigation of the underlying instabilities in  
28 relation to the leading geomorphological processes involved.

29 In this work, we focus on landscapes characterized by runoff  
30 erosion, expressed as a function of the specific drainage area  
31  $a$  (21) to obtain grid-independent solutions without the in-

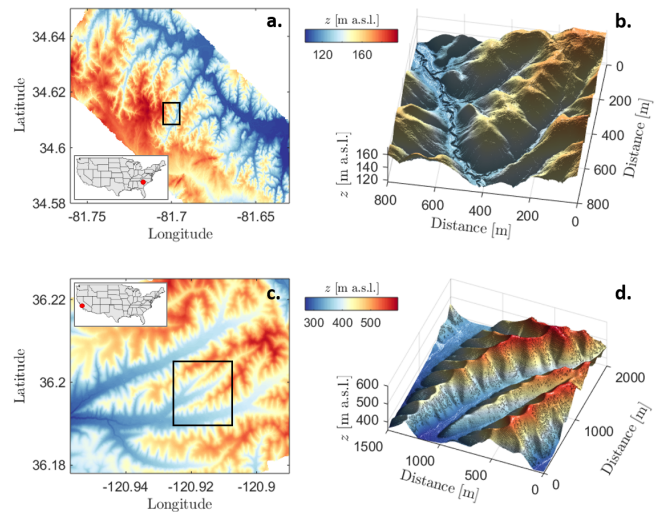


**Fig. 1. Ridge and valley patterns in natural landscapes.** 1-meter resolution LiDAR topographies of (a) the Calhoun Critical Zone landscape in South Carolina and (b) Gabilan Mesa in California. Panels b and d show three-dimensional surfaces for two subsets (black rectangles in panels a and c) where regular evenly spaced valleys are visible. Data were obtained from the National Center for Airborne Laser Mapping (NCALM) and retrieved from the OpenTopography facility.

32 introduction of additional system parameters. The resulting  
33 system of coupled, nonlinear partial differential equations  
34 (PDEs) provides a starting point for the theoretical analysis of  
35 channel-forming instabilities and landscape self-organization  
36 and allows us to describe the resulting ridge and valley pat-  
37 terns as a function of the relative proportions of diffusive soil

## Significance Statement

We show that a sequence of increasingly complex ridge and valley networks is produced by a system of nonlinear partial differential equations serving as a minimalist landscape evolution model describing the interplay between soil creep, runoff erosion, and tectonic uplift. We identify the critical conditions for the transition from a smooth to a channelized topography by means of a linear stability analysis and highlight striking similarities with fluid dynamic turbulence. The results shed light on the physical mechanisms responsible for observed landscape self-organization. The formation of regular pre-fractal networks reveals the tendency of the system to evolve towards optimal configurations typical of non-equilibrium complex systems.

Author contributions: S.B. and A.P. designed research, discussed results, and wrote the paper. S.B. and M.H. performed the numerical simulations, while S.B., C.C., and A.P. performed the linear stability analysis. All the authors reviewed and edited the final version of the manuscript.

The authors declare no conflict of interest.

<sup>1</sup>To whom correspondence should be addressed. E-mail: aporpora@princeton.edu

38 **creep, runoff erosion, and tectonic uplift.** The nonlocal character of the equations makes the boundary conditions extremely  
 39 important. On regular (i.e., square and rectangular) domains,  
 40 simulations reveal a sequence of channel instabilities reminiscent of the laminar-to-turbulent transition (22–24). The  
 41 explicit mathematical structure makes it possible to perform a  
 42 linear stability analysis of the coupled PDE system to identify  
 43 the critical conditions for the first channel-forming instability.  
 44 The subsequent branching sequence towards smaller and  
 45 smaller valleys until soil creep becomes dominant is similar  
 46 to the turbulent cascade with large scale vortices leading to  
 47 smaller ones until viscous dissipation. The formation of networks of ridges and valleys, brought about by the regular  
 48 boundary conditions, also reveals the tendency of the system  
 49 to develop configurations suggestive of optimization principles  
 50 (11) typical of non-equilibrium thermodynamics and complex  
 51 systems (16, 25–32). Our analysis is different from recent interesting contributions on groundwater-dominated landscapes  
 52 (33, 34), where branching and valley evolution is initiated at seepage points in the landscape.

## 58 Landscape evolution in detachment-limited conditions

59 The time evolution of the surface elevation  $z(x, y, t)$  is described by the sediment continuity equation (17, 18, 35, 36)

$$61 \quad \frac{\partial z}{\partial t} = U - \nabla \cdot \mathbf{f} = U - \nabla \cdot (\mathbf{f}_d + \mathbf{f}_c), \quad [1]$$

62 where  $t$  is time,  $U$  is the uplift rate, and  $\mathbf{f}$  is the total volumetric sediment flux, given by the sum of fluxes related to runoff erosion/channelized flow ( $\mathbf{f}_c$ ) and soil creep processes ( $\mathbf{f}_d$ ). The soil creep flux is assumed to be proportional to the topographic gradient (37, 38), hence  $\mathbf{f}_d = -D\nabla z$ ,  $D$  being a diffusion coefficient (here assumed to be constant in space and time).  
 66 In the so-called detachment-limited (DL) conditions (6, 18, 39) it is assumed that all eroded material is transported outside the model domain, so that no sediment redeposition occurs. Under these conditions, the runoff erosion term is approximated as a sink term given by (18)  $\nabla \cdot \mathbf{f}_c \approx K'_a |\nabla z|^n q^m$ , where  $K'_a$  is a coefficient,  $q$  is the discharge per unit width of contour line, and  $m$  and  $n$  are model parameters. As a result, Eq. (1) becomes

$$76 \quad \frac{\partial z}{\partial t} = D\nabla^2 z - K'_a q^m |\nabla z|^n + U. \quad [2]$$

77 Thus the soil creep flux results in a diffusion term which tends to smooth the surface, while the runoff erosion component is a sink term which excavates the topography as a function of local slope and specific water flux.

81 The surface water flux  $q$  is linked to the continuity equation

$$82 \quad \frac{\partial h}{\partial t} = R - \nabla \cdot (q\mathbf{n}) \quad [3]$$

83 where  $h$  is the water height,  $\mathbf{n}$  the direction of the flow, and  $R$  the rainfall rate effectively contributing to runoff production. Eq. (3) can be simplified assuming steady-state conditions with constant, representative rainfall rate,  $R_0$ , and (as in previous works (40)) constant speed of water flow  $v_0$  in the direction opposite to the landscape gradient (i.e.,  $\mathbf{n} = -\nabla z/|\nabla z|$ ). In such conditions, it can be shown (21) that the water height,  $h$ , and the specific water flux,  $q$ , are both proportional to the specific contributing area,  $a$ , i.e.  $h = q/v_0 = aR_0/v_0$ . As a

92 result, the system of Eqs. (3) - (2) reduces to an equation for the specific catchment area  $a$  (21),

$$94 \quad -\nabla \cdot \left( a \frac{\nabla z}{|\nabla z|} \right) = 1, \quad [4]$$

95 coupled to the landscape evolution equation

$$96 \quad \frac{\partial z}{\partial t} = D\nabla^2 z - K_a a^m |\nabla z|^n + U, \quad [5]$$

97 with an adjusted erosion constant  $K_a$  to account for the proportionality between  $a$  and  $q$ .

98 It is important to observe that the specific drainage area  $a$  has units of length and is related to the drainage area  $A$  as  $a = \lim_{w \rightarrow 0} A/w$ ; it is thus defined per unit width of contour line  $w$  (21). Most landscape evolution models (e.g., 9, 18, 41, 42) use the total drainage area  $A$  in Eq. (5) instead of  $a$ , with several notable implications. The value of  $A$  is generally evaluated using numerical flow-routing algorithms (e.g., D8, D $\infty$  (43)) which provide grid-dependent values of  $A$ . To correct for this, the drainage area  $A$  is often modified to account for the channel width (18, 41), but this results in approximations with arbitrary parameters. Conversely, the use of  $a$  avoids grid-dependence of the resulting topography. Moreover, re-casting the problem in terms of a consistent coupled system of PDEs makes it possible to analyze theoretically the landscape evolution process. As detailed below (see Methods), an analytic solution for the steady state hillslope profile can be derived (44) and then used as a basic state for a linear stability analysis to identify the critical conditions for the first channel formation and the characteristic valley spacing.

108 It is useful to non-dimensionalize the system of Eqs. (4) and (5) to quantify the relative impact of soil creep, runoff erosion, and uplift on the landscape morphology. Using a typical length scale of the domain,  $l$ , and the parameters of Eqs. (4) and (5), the following dimensionless quantities can be introduced:  $\hat{t} = \frac{tD}{l^2}$ ,  $\hat{x} = \frac{x}{l}$ ,  $\hat{y} = \frac{y}{l}$ ,  $\hat{z} = \frac{zD}{Ul^2}$ , and  $\hat{a} = \frac{a}{l}$ . With these quantities, Eq. (5) becomes

$$125 \quad \frac{\partial \hat{z}}{\partial \hat{t}} = \hat{\nabla}^2 \hat{z} - \mathcal{C}_{\mathcal{I}} \hat{a}^m |\hat{\nabla} \hat{z}|^n + 1 \quad [6]$$

126 where

$$127 \quad \mathcal{C}_{\mathcal{I}} = \frac{K_a l^{m+n}}{D^n U^{1-n}}. \quad [7]$$

128 As we will see later, this index describes the tendency to form channels in a way which is reminiscent of the global Reynolds number (defined as the ratio of inertial to viscous forces) in fluid mechanics, as well as of the ratio of flow permeabilities used in constructal theory (45). A similar quantity based on a local length scale (i.e., the mean elevation of the emerging topographic profile) was used in Perron et al. (18). The definition of  $\mathcal{C}_{\mathcal{I}}$  as a function of global variables based on system parameters (e.g., uplift rate  $U$ ) and boundary conditions allows us to directly infer system behavior. For example, when the slope exponent  $n$  is equal to 1, the relative proportion of runoff erosion and soil creep can be seen to be independent of the uplift rate; however, if  $n > 1$  the uplift acts to increase the runoff erosion component, while for  $n < 1$  it enhances the diffusive component of the system. As we will see, this results in different drainage-network patterns as a function of uplift rates.

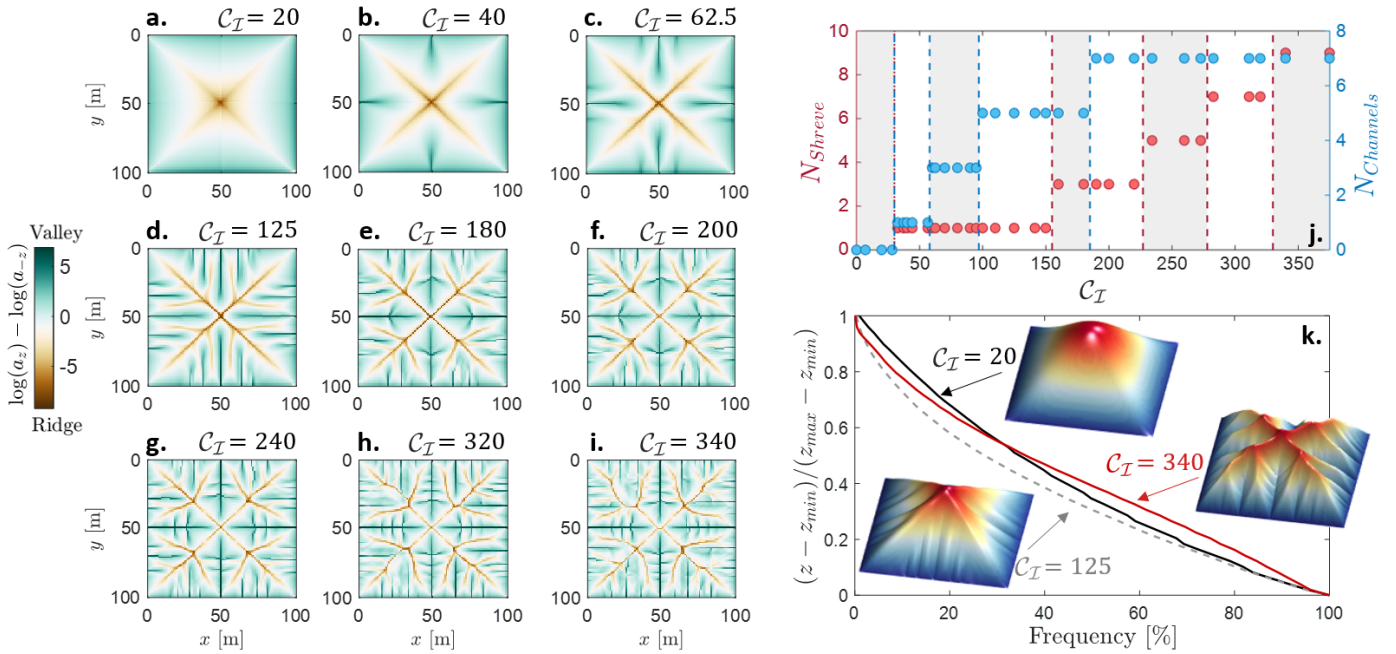


**Fig. 2. Channelization cascade.** Simulation results obtained for  $m = 0.5$  and  $n = 1$ . (a-i) Ridge and valley patterns obtained for  $C_I$  values equal to 20, 40, 62.5, 125, 180, 200, 240, 320, and 340: brown corresponds to ridges and green to valleys. To better highlight the ridge and valley structure we show here the difference between the specific drainage area  $a$  and the specific dispersal area  $a_{-z}$  (i.e., the value of  $a$  computed over the flipped topography - see ref. 20). (j) Highest Shreve order (red) and number of main channels on each domain side (blue) for different values of the dimensionless parameter  $C_I$ . Based on the number of channels and the Shreve order nine regimes can be identified with distinctively different ridge/valley patterns (shown in panels a-i). (k) Normalized hypsometric curves obtained for  $C_I = 20$  (solid black), 125 (dashed gray), and 340 (solid red): when no secondary branching is observed (i.e.,  $C_I \lesssim 155$ ) the hypsometric curve is concave, while after the first secondary branching is formed it undergoes a transition to a shape concave for higher elevations and convex at low elevations. Insets in panel k show 3d plots of the steady state topographies for the three cases, the color code represents surface elevation (red = high, blue = low).

## Results

**Organized ridge and valley patterns.** Simulation results obtained by numerically solving Eqs. (4)-(5) over square domains with  $m = 0.5$  and  $n = 1$  (see Methods for details) are shown in Fig. 2. The emerging ridge/valley patterns are classified in terms of Shreve order (used here as a measure of branching complexity - see ref. 3), and number of channels formed on each side of the domain. As can be seen from Eq. (7), for  $n = 1$  the dimensionless parameter  $C_I$  is independent of the uplift rate, so that the spatial patterns of Fig. 2 are only a function of the relative proportions of the soil creep and runoff erosion components. For low  $C_I$  values (i.e.,  $\lesssim 30$ ) no channels are formed and the topography evolves to a smooth surface dominated by diffusive soil creep (Fig. 2a). As the runoff erosion coefficient is increased the system progressively develops one, three, and five channels on each side of the square domain for  $30 \lesssim C_I \lesssim 58$ ,  $58 \lesssim C_I \lesssim 97$ , and  $97 \lesssim C_I \lesssim 155$ , respectively (Fig. 2b-d). When  $C_I$  is increased above  $\approx 155$  the central channels develop secondary branches, with the main central channel becoming of Shreve order three (Fig. 2e). As  $C_I$  is further increased seven channels can be observed originating on each side of the domain, and the main central channel further branches (Fig. 2f-i) becoming of order nine for the highest  $C_I$  used for this configuration.

As the resulting landscape changes from a smooth topography to a progressively more dissected one, the shape of the hypsometric curve varies from concave (i.e., slope decreases along the horizontal axis) to one with a convex portion for low elevations (Fig. 2k). In particular, channel formation (with no secondary branching) causes the hypsometric curve

to progressively lower as a result of the lower altitudes observed in the topography, while maintaining a concave profile. As secondary branches develop, the hypsometric curve shifts to a concave/convex one, with the convex portion at lower altitudes becoming more evident as  $C_I$  increases (see red line for  $C_I = 340$  in Fig. 2k).

The striking regularity of the drainage and ridge patterns induced by the simple geometry of the domain is reminiscent of regular pre-fractal structures (e.g., Peano basin (8, 9, 46-48)) and is indicative of the fundamental role of boundary conditions due to the highly non-local control introduced by the drainage area term. The introduction of noise and irregular boundaries quickly breaks the regularity of the patterns (see results from numerical simulations obtained over progressively more irregular boundaries in the SI Appendix, Fig. S10). The ridge and valley networks of Fig. 2 highly resemble Fig. 5 in ref. 31, where optimized tree-shaped flow paths were constructed to connect one point to many points uniformly distributed over an area. We further highlight similarities with the patterns obtained in ref. 30 by means of an erosion model where the global flow resistance is minimized.

**Effect of runoff erosion laws.** The effect of different runoff erosion laws has been discussed in the literature (42) also in relation to climate, vegetation cover, and soil properties (49, 50). Their role was analyzed here by changing the values of the exponents  $n$  and  $m$ , as shown in Fig. 3.

When the value of  $n$  is different from unity, the resulting ridge/valley patterns depend on the uplift rate  $U$ , as per Eq. (7). When  $n$  is increased the system displays channelization and secondary branching for higher values of  $C_I$  (i.e.,

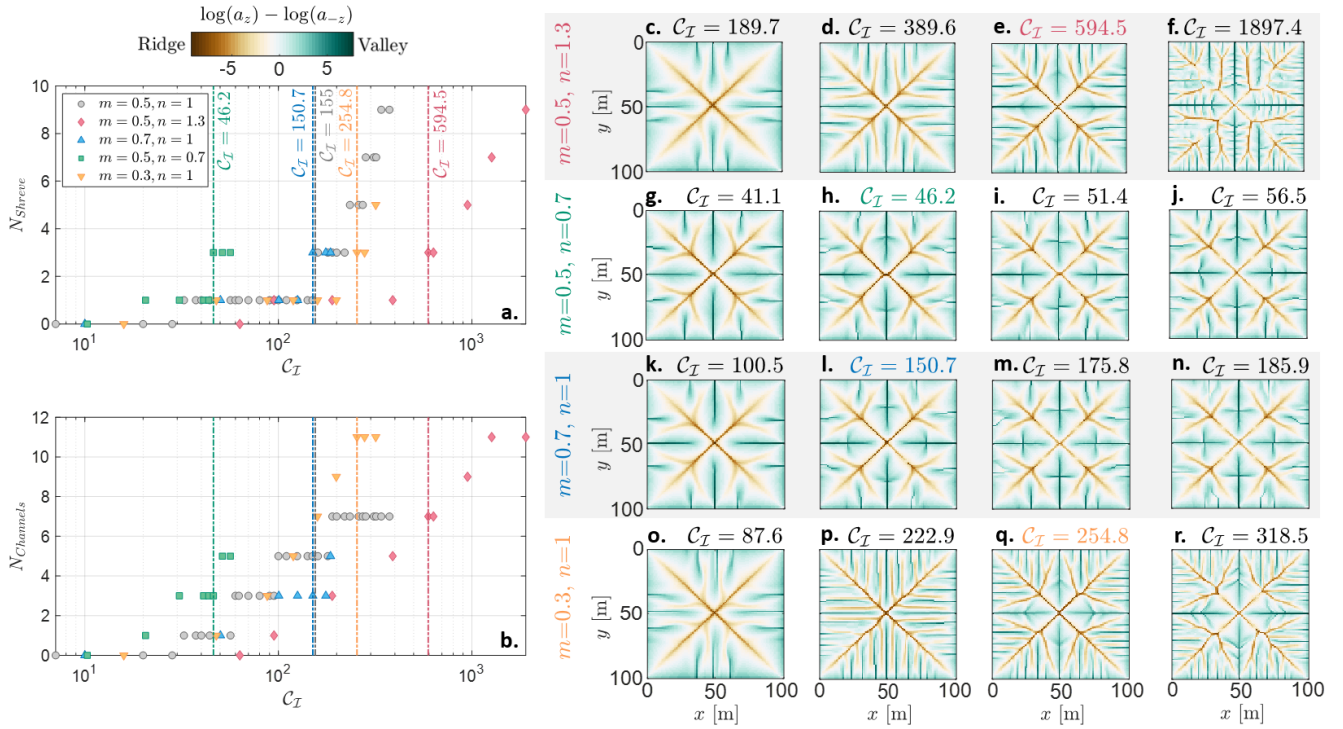


**Fig. 3. Effect of runoff erosion laws.** Simulation results obtained for different values of the slope and runoff exponents (i.e.,  $n$  and  $m$ ): (a) maximum Shreve order and (b) number of channels on each domain side as a function of  $C_I$ . Colored dash-dotted lines mark the  $C_I$  values at which the first secondary branching is observed for each set of  $m$  and  $n$  values, and the corresponding ridge/valley patterns are highlighted in panels c-r. (c-r) Examples of two-dimensional ridge (brown) and valley (green) patterns for scenarios with (c-f) increased slope exponent ( $n = 1.3, m = 0.5$ , and  $C_I = 189.7, 389.6, 594.5, 1897.4$ ), (g-j) decreased slope exponent ( $n = 0.7, m = 0.5$ , and  $C_I = 41.1, 46.2, 51.4, 56.6$ ), (k-n) increased water flux exponent ( $n = 1, m = 0.7$ , and  $C_I = 100.5, 150.7, 175.8, 185.9$ ), and (o-r) decreased water flux exponent ( $n = 1, m = 0.3$ , and  $C_I = 87.6, 222.9, 254.8, 318.5$ ).

points are shifted to the right in Fig. 3a,b), with a more dissected planar geometry characterized by narrower valleys and smaller junction angles (Fig. 3c-f). A decrease in  $n$  leads to smoother geometries with wider valleys and the first secondary branching developing when only three channels per each side of the domain are present (see Fig. 3g-j). This results in a hypsometric curve with a more pronounced basal (i.e., at low altitudes) convexity for  $n > 1$ , as a consequence of the progressively more dissected topography (see SI Appendix, Fig. S2).

As  $m$  is increased (Fig. 3k-n) the system develops secondary branching when only three channels are present on each side of the domain, with the formation of less numerous but wider valleys with higher junction angles, and a reduced basal convexity in the hypsometric curve (see SI Appendix, Fig. S2). Conversely, a decrease in  $m$  results in a more dissected landscape, with narrower valleys (Fig. 3o-r) and a more pronounced transition of the hypsometric curve to a convex shape for low altitudes (see SI Appendix, Fig. S2).

**Wide rectangular domains.** To assess boundary-condition effects on branching patterns we also considered very wide rectangular domains ( $C_I$  is constructed using the distance between the longest sides). Besides numerical investigation, in this case an analytical solution is possible for the unchanneled case (for  $m = 1$  and  $n = 1$ , see Methods), around which we also performed a linear stability analysis. In our analogy with turbulent flows, the case of wide rectangular domains corresponds to the flow of viscous fluids between parallel plates (23, 24).

Results from the linear stability analysis are shown in Fig. 4. A critical value  $C_{I,c} \approx 37$  for the first channel instability is identified, corresponding to a characteristic valley spacing  $\lambda_c$  of approximately 42 m, in line with observations (an analysis of five landscapes in the continental US from ref. 51 provides values of valley spacing ranging between approximately 30 and 300 m). As  $C_I$  further increases (i.e., runoff erosion increases with respect to diffusion) the predicted valley spacing is reduced (see Fig. 4c), with the formation of progressively narrower valleys. Results from the linear stability analysis are in line with predictions from numerical experiments conducted over large rectangular domains, where the first channel instability occurs at  $C_{I,c} \approx 32$  with a valley spacing  $\lambda_c \approx 33$  m. Analogously to the Orr-Sommerfeld problem for plane Poiseuille flow, the system here presents a Type I linear instability (52). Insight on the role of the  $m$  and  $n$  exponents on the critical channelization index  $C_{I,c}$  and related valley spacing was obtained from numerical experiments. As shown in the SI Appendix (Fig. S9), as the water flow exponent  $m$  decreases, the value of  $C_I$  at which the first channel forming instability occurs increases and the valley spacing decreases. This is in agreement with results obtained over square domains (Fig. 3) where a decrease in the value of  $m$  resulted in a more dissected landscape with narrower valleys.

The numerical simulations confirm the results of the linear stability analysis and are in agreement with those of ref. 18. Fig. 5 compares the drainage patterns obtained as a function of  $C_I$  for rectangular domains of size 100 m by 500 m. As for the square domain, for small  $C_I$  values the soil creep component dominates resulting in an unchanneled smooth topography

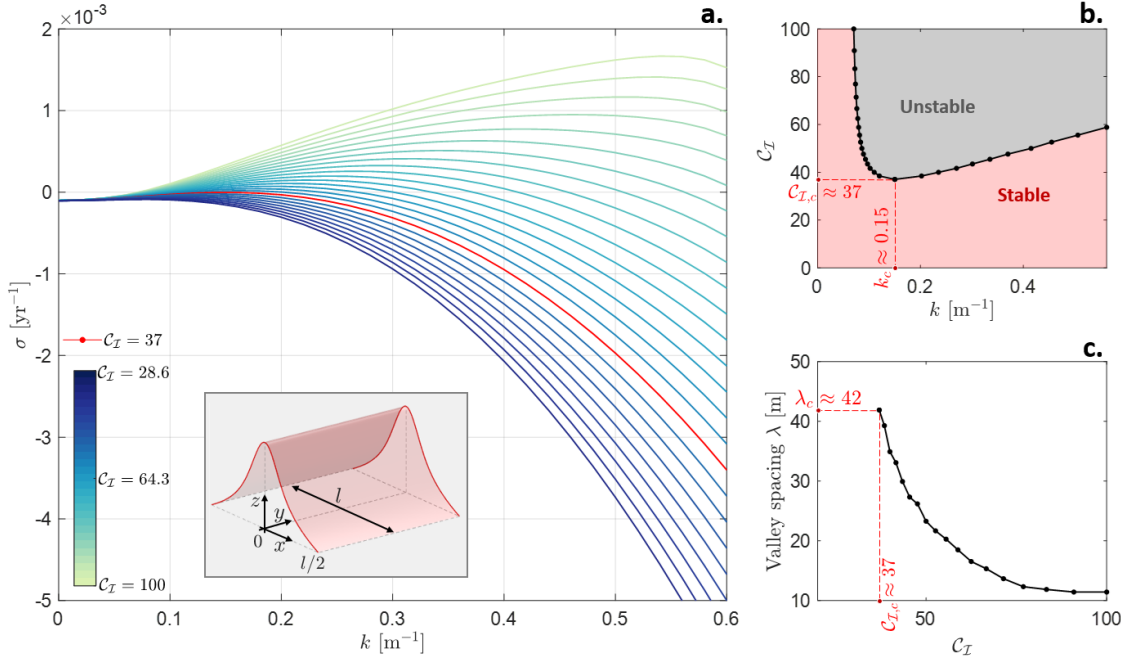


**Fig. 4. Linear stability analysis.** (a) Growth rate  $\sigma$  as a function of wavenumber  $k$  for different values of the dimensionless number  $C_I$ , (b) marginal stability curve (the solid line marks the instability of the basic state to channel initiation), and (c) characteristic valley spacing  $\lambda$  as a function of the dimensionless number  $C_I$ . The linear stability analysis predicts a critical value  $C_{I,c} \approx 37$  for the first channel instability (with valley spacing  $\lambda_c \approx 42$  m). The inset in panel (a) shows the geometry assumed as a basic state for the linear stability analysis and for the derivation of the theoretical hillslope profiles (see also Methods).

264 (Fig. 5a). After the first channelization, valleys tend to  
 265 narrow as  $C_I$  increases until the first secondary branching  
 266 occurs (Fig. 5b,c). Further increasing the runoff erosion  
 267 component provides progressively more dissected landscapes  
 268 with the emergence of secondary branching (Fig. 5d-f). As  
 269 in turbulent flows larger Reynolds numbers produce smaller  
 270 and smaller vortices, here increasing  $C_I$  leads to finer and finer  
 271 branching (the resolution of which becomes quickly prohibitive  
 272 from a computational standpoint).

273 The mean elevation profiles, computed as average elevation  
 274 values along the  $x$  axis and neglecting the terminal parts of  
 275 the domain to avoid boundary effects, are shown in Fig. 5g-l.  
 276 As the topography becomes progressively more dissected with  
 277 increasing  $C_I$ , the mean elevation profile tends to become more  
 278 uniform (Fig. 5g-l). Such a behavior of the mean elevation  
 279 profiles for increasing  $C_I$  is similar to the flattening of turbulent  
 280 mean velocity profiles with increasing Reynolds number (24).

281 The transition from a smooth to a channelized topography  
 282 with increasing  $C_I$  is reflected in the behavior of the quantity  
 283  $DS_*/Ul = f(C_I, m)$ , which describes the ratio of the outgoing  
 284 diffusive flux and the incoming uplift sediment flux at the hill-  
 285 slope base,  $S_*$  being the slope of the mean elevation profile at  
 286 the hillslope base (see Methods for details). Fig. 5p shows the  
 287 relationship between  $DS_*/Ul$  and  $C_I$  obtained from numerical  
 288 simulations for  $n = 1$  and different values of the exponent  $m$ .  
 289 For small  $C_I$  values the numerical results match the analytic  
 290 relationship for the smooth surface (Eq. (11)) and deviate  
 291 from it at  $C_{I,c} \approx 32$  where the first channel-forming instability  
 292 occurs. Continuing our analogy with turbulence, the behavior  
 293 of  $DS_*/Ul$  as a function of  $C_I$  closely resembles that of the  
 294 friction factor with increasing Reynolds number (see Methods  
 295 as well as figure 7.3 in ref. 53).

296 The effect of boundary conditions on the spatial regularity  
 297 of ridge and valley patterns becomes especially apparent when  
 298 comparing simulations with different aspect ratios. As can be  
 299 seen in Fig. 5m-o, when the domain size is slightly changed,  
 300 the spatial organization of ridges and valleys is modified (see,

e.g., the more regular pattern obtained for  $\beta = 4.6$  compared to  
 $\beta = 5.1$ ), while the mean elevation profiles remain practically  
 invariant (see SI Appendix, Fig. S8). This suggests that  
 some optimal domain length is needed to accommodate the  
 formation of regular ridge and valley patterns (this is also  
 evident from an analysis of cross-sections along the longer  
 sides of the domain, see Figs. S3-S7 in the SI Appendix). This  
 results in the formation of dislocation defects, as highlighted  
 in the example of Fig. 5m-o, as it is typical in nonlinear  
 pattern-forming PDEs (52).

## Discussion and conclusions

A succession of increasingly complex networks of ridges and  
 valleys was produced by a system of nonlinear PDEs serving  
 as a minimalist model for landscape evolution in detachment-  
 limited conditions. The sequence of instabilities is reminiscent  
 of the subsequent bifurcations in fluid dynamic instabilities  
 (23, 24, 52) and is captured by a dimensionless number ( $C_I$ )  
 accounting for the relative importance of runoff erosion, soil  
 creep, and uplift in relation to the typical domain size. Tan-  
 talizing analogies with fluid turbulence, and in general with  
 other driven non-equilibrium systems in which a hierarchical  
 pattern develops toward finer scales, can also be observed in  
 the competition between runoff erosion and soil creep (which  
 resembles the competition between viscous and inertial forces),  
 the reduction of the minimum branching scale with  $C_I$ , and  
 the flattening of the mean hypsometric curves as the channel-  
 ization is increased.

Characteristic spatial configurations were shown to emerge  
 over both square and rectangular domains from the trade-  
 off between diffusion and erosion. The striking regularity  
 of the ridge and valley networks, with the characteristics  
 of regular pre-fractals (e.g., the Peano basin (8, 46-48)), is  
 quickly lost as effects of noise and irregular boundaries are  
 introduced (see SI Appendix, Fig. S10). The shape of the  
 hypsometric curve depends on the level of channelization and

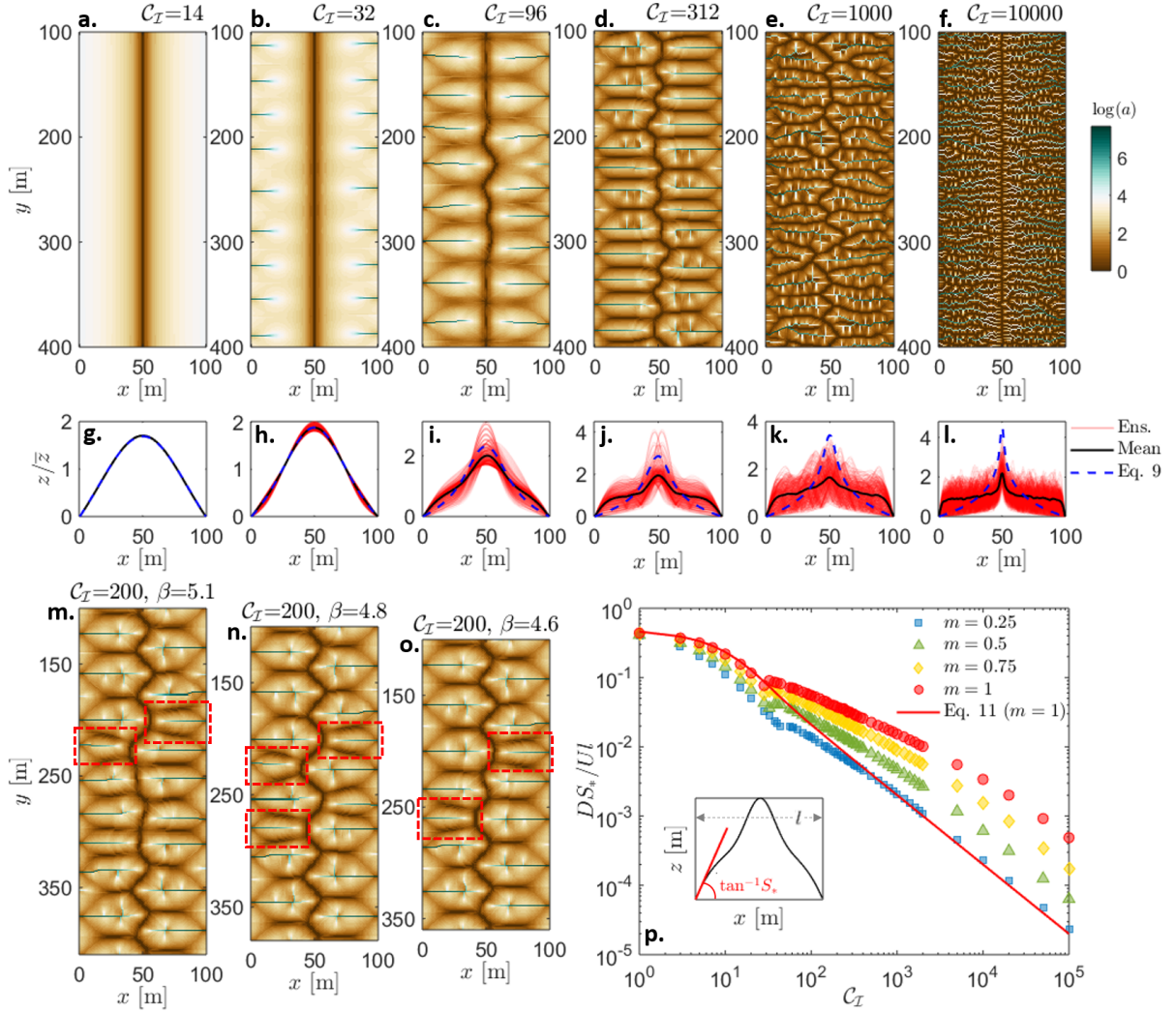


**Fig. 5. Rectangular domains.** Ridge/valley networks obtained for  $m = n = 1$  over rectangular domains with (a-f)  $\beta = 5$  ( $C_T = 14, 32, 96, 312, 1000,$  and  $10000$ ), (m)  $\beta = 5.1$  ( $C_T = 200$ ), (n)  $\beta = 4.8$  ( $C_T = 200$ ), and (o)  $\beta = 4.6$  ( $C_T = 200$ ).  $\beta$  is a shape factor defined as the ratio between the two horizontal length scales  $l_y$  and  $l_x$ , namely  $\beta = l_y/l_x$ . Examples of dislocation defects are shown by the red dashed rectangles in panels m-o. (g-l) Normalized elevation profiles along the  $x$  axis for the six simulations of panels a-f: black lines are the mean elevation profiles, red lines show the ensemble of all the profiles along  $x$ , blue dashed lines are analytical elevation profiles for the unchanneled case – Eq. (9). Mean elevation profiles along the  $x$  axis were computed as average values of the elevation profiles neglecting the extremal parts (100 m length) of the domain. (p) Slope of the mean elevation profile  $S_*$  as a function of  $C_T$  for simulations with  $n = 1$  and  $m = 0.25, 0.5, 0.75,$  and  $1$ . The solid red line represents the analytical solution for  $m = 1$  (Eq. (11)) for the unchanneled case. The schematic in the inset shows the definition of  $S_*$  and  $l$  used in the vertical axis of the chart.

336 branching (54) and thus on the dominant erosional mechanisms  
 337 acting on the landscape (i.e., interplay between runoff erosion,  
 338 soil creep, and uplift) and the various landscape properties  
 339 affecting diffusion and erosion coefficients, such as soil type,  
 340 vegetation cover, and climate. When diffusion dominates,  
 341 hypsometric curves display a less pronounced basal convexity  
 342 (54). A systematic analysis of real topographies in terms of  
 343 statistics of hypsometry, branching angles, and characteristic  
 344 spacing would help infer values of  $C_T$  and the non-linearity  
 345 exponents  $m$  and  $n$  of natural landscapes, and possibly link  
 346 them to the abiotic and biotic properties of the landscape  
 347 under consideration.

348 It will also be interesting to explore the differences in tran-  
 349 sient dynamics between the hypsometry of juvenile and old  
 350 landscapes. It is likely that, during the early stages of the  
 351 basin development when the drainage network is formed, the  
 352 hypsometric curve presents a more pronounced basal convexity

(2) regardless of the value of  $C_T$ , progressively transitioning  
 toward its quasi-equilibrium form during the “relaxation phase”  
 (55). Such slow relaxations (e.g., Fig. 5), often towards slightly  
 irregular configurations rather than perfectly regular networks,  
 are reminiscent of the presence of defects in crystals and the  
 amorphous configurations originating in glass transition (56).

## Materials and Methods

**Analytical solutions for  $m = n = 1$ .** To derive one-dimensional  
 steady state solutions of the coupled PDE system (Eqs. (4)-(5)) we  
 consider a symmetric hillslope of length  $l$  in the  $x$ -direction,  
 with divide at  $x = 0$  (see inset in Fig. 4a). Assuming a fixed  
 elevation  $z = 0$  at  $x = \pm l/2$ , the steady steady solution of the  
 coupled system

366 of Eqs. (4) and (5) for  $m = n = 1$  reads (44)

$$367 \quad a_0 = |x| \quad [8]$$

$$368 \quad z_0 = \frac{U}{2D} \left[ \left( \frac{l}{2} \right)^2 \mathcal{H} \left( 1, 1; \frac{3}{2}, 2; -\frac{K_a \left( \frac{l}{2} \right)^2}{D} \right) \right. \\ 369 \quad \left. - x^2 \mathcal{H} \left( 1, 1; \frac{3}{2}, 2; -\frac{K_a x^2}{D} \right) \right] \quad [9]$$

370 where subscript 0 denotes the basic steady state, and  $\mathcal{H}(\cdot, \cdot; \cdot, \cdot; \cdot)$  is  
371 the generalized hypergeometric function (57). In these conditions,  
372 the local slope  $S_0 = dz_0/dx$  can also be derived analytically as (44)

$$373 \quad S_0 = \frac{\sqrt{2UD} \left( \frac{\sqrt{K_a x}}{\sqrt{2D}} \right)}{\sqrt{DK_a}} \quad [10]$$

374 where  $\mathcal{D}(\cdot)$  is the Dawson's integral (57).

375 **Linear stability analysis.** We studied the stability of the basic state  
376 (Eqs. (8)-(9)) to perturbations  $\tilde{a}$  and  $\tilde{z}$  in the  $y$ -direction. Boundary  
377 conditions are zero sediment and specific drainage area at the  
378 hilltop ( $\tilde{a} = d\tilde{z}/dx = 0$  at  $x = 0$ ) and fixed elevation at the domain  
379 boundary ( $\tilde{z} = 0$  at  $x = l/2$ ). We use normal mode analysis  
380 and write perturbations in the classical form  $\tilde{a} = \phi(x)e^{iky+\sigma t}$  and  
381  $\tilde{z} = \psi(x)e^{iky+\sigma t}$  (plus complex conjugate), where  $k$  and  $\sigma$  are the  
382 wavenumber and the growth rate of the perturbations, respectively.  
383 The perturbed system can be re-cast in terms of a third order  
384 non-constant coefficient differential eigenvalue problem of the form  
385  $\gamma_1(x)\phi''''(x) + \gamma_2(x)\phi'''(x) + \gamma_3(x)\phi''(x) + \gamma_4(x)\phi'(x) = \sigma\gamma_5(x)\phi'(x)$ .  
386 Solutions to the stability problem are obtained by means of a spectral  
387 Galerkin technique with numerical quadrature (58, 59). Among the  
388 discrete set of eigenvalues obtained, we tracked the behavior of the  
389 least stable (i.e., with largest real part). The stability analysis was  
390 performed here for unitary exponents  $m$  and  $n$  due to the availability  
391 of an analytical form of the basic state. Numerical results for a  
392 wider range of  $m$  and  $n$  values are reported in the SI Appendix (Fig.  
393 S9).

394 **Numerical simulations.** Numerical simulations were performed using  
395 forward differences in time and centered difference approximations  
396 for the spatial derivatives, considering regular square grids of lateral  
397 dimension  $l$ , as well as on rectangular domains with shape factor  
398  $\beta$ , defined as the ratio between the domain dimensions in the  $y$   
399 and  $x$  direction (i.e.,  $\beta = l_y/l_x$ ). Specifically, in the simulations  
400 over rectangular domains we fixed the length in the  $x$  direction (i.e.,  
401  $l_x = 100$  m), and varied only the length  $l_y$  in the  $y$  direction. The  
402 total drainage area  $A$  was computed at each grid point with the  $D\infty$   
403 algorithm, while  $a$  was then approximated as  $A/\Delta x$  (43, 60), with  
404  $\Delta x$  the grid size. Simulations were run assuming  $\Delta x = 1$  m (addi-  
405 tional numerical experiments, shown in the SI Appendix (Fig. S1),  
406 were performed for different grid sizes to validate the independence  
407 of the resulting patterns on the grid resolution). Convex profiles  
408 were used as initial condition. Over wide rectangular domains for  
409  $C_T \geq 320$  a white noise with standard deviation equal to  $10^{-6}$  m  
410 was also added in the initial condition. A sensitivity analysis was  
411 conducted over square domains (not shown) to make sure that the  
412 resulting spatial organization of ridges and valleys at steady state  
413 was robust to the choice of initial conditions. We considered a wide  
414 range of  $C_T$  values (from  $10^0$  to  $10^5$ ) constructed by using literature  
415 values of the system parameters, which are generally estimated in  
416 terms of time-averaged values from experimental hillslope shapes  
417 (61) or high resolution topographies (18, 19).

418 **Dimensional analysis of the channelization transition.** We proceed  
419 similarly to the analysis of turbulence transition in pipes and chan-  
420 nels. There the relationship between the friction factor  $\xi$  and the  
421 Reynolds number  $Re$  can be obtained by first relating the wall  
422 shear stress  $\tau = \mu \bar{u}/dx^*|_{x^*=0}$ , where  $\bar{u}$  is the streamwise mean  
423 velocity profile and  $x^*$  is the distance from the wall, to its governing  
424 quantities as  $\tau = \Xi(V, L, \mu, \rho, \epsilon)$ , where  $\rho$  is the density,  $\mu$  the vis-  
425 cosity,  $V$  the mean velocity,  $L$  the characteristic lateral dimension,  
426 and  $\epsilon$  the roughness height. The Pi-Theorem then may be used to  
427 express the head loss per unit length ( $g$  is gravitational acceleration)  
428 as  $S_h = \frac{4\tau}{\rho g L} = \frac{V^2}{2gL} \xi \left( Re, \frac{\epsilon}{L} \right)$ , see ref. 62. Analogously, here we

429 can relate the slope of the mean elevation profile at the hillslope  
430 base  $S_* = d\bar{z}/dx|_{x=l/2}$  to the parameters and characteristics of the  
431 landscape evolution model as  $S_* = \Phi(D, K_a, m, U, l)$  (we consider  
432 here  $n = 1$ ). Choosing  $l$ ,  $U$ , and  $D$  as dimensionally independent  
433 variables, the Pi-Theorem yields  $DS_*/Ul = \varphi(C_T, m)$ , where the  
434 quantity  $DS_*$  quantifies the diffusive outgoing sediment flux per  
435 unit width (along the  $x$ -axis) at the boundary, while the term  $Ul$   
436 represents the incoming sediment flux by tectonic uplift per unit  
437 width. Such a functional relationship can be analytically derived  
438 for the unchanneled case when  $m = 1$  from Eq. (10) as

$$439 \quad \frac{DS_*}{Ul} = \left( \frac{C_T}{2} \right)^{-1/2} \mathcal{D} \left[ \left( \frac{C_T}{8} \right)^{1/2} \right]. \quad [11]$$

440 In the numerical simulations,  $S_*$  was computed as the slope of the  
441 linear fit to the mean elevation profile in the first 3 meters at the  
442 hillslope base (see inset in Fig. 5p).

443 **Data and code availability.** 1-meter resolution LiDAR data for Cal-  
444 houn and Gabilan Mesa can be downloaded from the OpenTopog-  
445 raphy facility (<https://opentopography.org>). The code used for the  
446 numerical simulations is described in ref. 63 and available on GitHub  
447 (<https://github.com/ShashankAnand1996/LEM>).

448 **ACKNOWLEDGMENTS.** We acknowledge support from the US  
449 National Science Foundation (NSF) grants EAR-1331846 and EAR-  
450 1338694, and BP through the Carbon Mitigation Initiative (CMI)  
451 at Princeton University. The useful comments of the anonymous  
452 reviewers are also gratefully acknowledged. LiDAR data for Calhoun  
453 and Gabilan Mesa were obtained from the National Center for  
454 Airborne Laser Mapping (NCALM) with support from the US  
455 National Science Foundation (EAR-1339015, EAR-1331846, EAR-  
456 1043051) and retrieved from <https://opentopography.org>.

- 457 1. R E Horton. Erosional development of streams and their drainage basins; hydrophysical  
458 approach to quantitative morphology. *Geological Society of America Bulletin*, 56(3):275–370,  
459 1945.
- 460 2. A N Strahler. Hypsometric (area-altitude) analysis of erosional topography. *Geological Soci-  
461 ety of America Bulletin*, 63(11):1117–1142, 1952.
- 462 3. R L Shreve. Statistical law of stream numbers. *The Journal of Geology*, 74(1):17–37, 1966.
- 463 4. T R Smith and F P Bretherton. Stability and the conservation of mass in drainage basin  
464 evolution. *Water Resources Research*, 8:1506–1529, 1972.
- 465 5. D S Loewenherz. Stability and the initiation of channelized surface drainage: a reassessment  
466 of the short wavelength limit. *Journal of Geophysical Research: Solid Earth*, 96(B5):8453–  
467 8464, 1991.
- 468 6. N Izumi and G Parker. Inception of channelization and drainage basin formation: upstream-  
469 driven theory. *Journal of Fluid Mechanics*, 283:341–363, 1995.
- 470 7. D G Tarboton, R L Bras, and I Rodriguez-Iturbe. The fractal nature of river networks. *Water  
471 Resources Research*, 24(8):1317–1322, 1988.
- 472 8. A Marani, R Rigon, and A Rinaldo. A note on fractal channel networks. *Water Resources  
473 Research*, 27(12):3041–3049, 1991.
- 474 9. I Rodriguez-Iturbe and A Rinaldo. *Fractal river basins: chance and self-organization*. Cam-  
475 bridge University Press, 2005.
- 476 10. P S Dodds and D H Rothman. Scaling, universality, and geomorphology. *Annual Review of  
477 Earth and Planetary Sciences*, 28(1):571–610, 2000.
- 478 11. R Rigon, A Rinaldo, I Rodriguez-Iturbe, R L Bras, and E Ijiaz-Vasquez. Optimal channel  
479 networks: a framework for the study of river basin morphology. *Water Resources Research*,  
480 29(6):1635–1646, 1993.
- 481 12. J R Banavar, F Colaiori, A Flammini, A Giacometti, A Maritan, and A Rinaldo. Sculpting of a  
482 fractal river basin. *Physical Review Letters*, 78(23):4522, 1997.
- 483 13. E Somfai and L M Sander. Scaling and river networks: A Landau theory for erosion. *Physical  
484 Review E*, 56(1):R5, 1997.
- 485 14. R Pastor-Satorras and D H Rothman. Scaling of a slope: the erosion of tilted landscapes.  
486 *Journal of Statistical Physics*, 93(3-4):477–500, 1998.
- 487 15. S Kramer and M Marder. Evolution of river networks. *Phys. Rev. Lett.*, 68:205–208, 1992.
- 488 16. A Arneodo, F Argoul, E Bacry, J F Muzy, and M Tabard. Golden mean arithmetic in the fractal  
489 branching of diffusion-limited aggregates. *Physical review letters*, 68(23):3456, 1992.
- 490 17. A Fowler. *Mathematical geoscience*. Springer Science & Business Media, 2011.
- 491 18. J T Perron, W E Dietrich, and J W Kirchner. Control on the spacing of first-order valleys.  
492 *Journal of Geophysical Research*, 113:F04016, 2008.
- 493 19. J T Perron, P W Richardson, K L Ferrier, and M Lapôtre. The root of branching river networks.  
494 *Nature*, 492(7427):100, 2012.
- 495 20. J C Gallant and M F Hutchinson. A differential equation for specific catchment area. *Water  
496 Resources Research*, 47(5), 2011.
- 497 21. S Bonetti, A D Bragg, and A Porporato. On the theory of drainage area for regular and  
498 non-regular points. *Proc. R. Soc. A*, 474(2211):20170693, 2018.
- 499 22. S B Pope. *Turbulent Flows*. Cambridge University Press, Cambridge, UK, 2000.
- 500 23. P G Drazin and W H Reid. *Hydrodynamic Stability*. Cambridge Mathematical Library. Cam-  
501 bridge University Press, 2 edition, 2004. .
- 502 24. P K Kundu, I M Cohen, and D W Dowling. *Fluid Mechanics 5th ed*. Elsevier, 2011.



503 25. A Rinaldo, A Maritan, F Colaiori, A Flammini, R Rigon, I Rodríguez-Iturbe, and J R Banavar.  
504 Thermodynamics of fractal networks. *Physical Review Letters*, 76(18):3364, 1996.

505 26. H Ozawa, A Ohmura, R D Lorenz, and T Pujol. The second law of thermodynamics and the  
506 global climate system: A review of the maximum entropy production principle. *Reviews of*  
507 *Geophysics*, 41(4), 2003.

508 27. L M Martyushev and V D Seleznev. Maximum entropy production principle in physics, chem-  
509 istry and biology. *Physics reports*, 426(1):1–45, 2006.

510 28. D Bensimon, L P Kadanoff, S Liang, B I Shraiman, and C Tang. Viscous flows in two dimen-  
511 sions. *Reviews of Modern Physics*, 58(4):977, 1986.

512 29. L M Sander and E Somfai. Random walks, diffusion limited aggregation in a wedge, and  
513 average conformal maps. *Chaos: An Interdisciplinary Journal of Nonlinear Science*, 15(2):  
514 026109, 2005.

515 30. M R Errera and A Bejan. Deterministic tree networks for river drainage basins. *Fractals*, 6  
516 (03):245–261, 1998.

517 31. S Lorente, W Wechsato, and A Bejan. Tree-shaped flow structures designed by minimizing  
518 path lengths. *International Journal of Heat and Mass Transfer*, 45(16):3299–3312, 2002.

519 32. A Bejan. *Advanced engineering thermodynamics*. John Wiley & Sons, 2016.

520 33. O Devauchelle, A P Petroff, H F Seybold, and D H Rothman. Ramification of stream networks.  
521 *Proceedings of the National Academy of Sciences*, 109(51):20832–20836, 2012.

522 34. R Yi, Y Cohen, H Seybold, E Stansifer, R McDonald, M Mineev-Weinstein, and D H Rothman.  
523 A free-boundary model of diffusive valley growth: theory and observation. *Proc. R. Soc. A*,  
524 473(2202):20170159, 2017.

525 35. W E Dietrich, D G Bellugi, L S Sklar, J D Stock, A M Heimsath, and J J Roering. Geomorphic  
526 transport laws for predicting landscape form and dynamics. *Prediction in Geomorphology*,  
527 pages 103–132, 2003.

528 36. T R Smith. A theory for the emergence of channelized drainage. *Journal of Geophysical*  
529 *Research: Earth Surface*, 115(F2), 2010.

530 37. W E H Culling. Analytical theory of erosion. *The Journal of Geology*, 68(3):336–344, 1960.

531 38. W E H Culling. Soil creep and the development of hillside slopes. *The Journal of Geology*,  
532 71(2):127–161, 1963.

533 39. A D Howard. A detachment-limited model of drainage basin evolution. *Water Resources*  
534 *Research*, 30(7):2261–2285, 1994.

535 40. I Rodríguez-Iturbe, A Rinaldo, R Rigon, R L Bras, A Marani, and E Ijász-Vásquez. Energy  
536 dissipation, runoff production, and the three-dimensional structure of river basins. *Water*  
537 *Resources Research*, 28(4):1095–1103, 1992.

538 41. J D Pelletier. Fluvial and slope-wash erosion of soil-mantled landscapes: detachment-or  
539 transport-limited? *Earth Surface Processes and Landforms*, 37(1):37–51, 2012.

540 42. A Chen, J Darbon, and J-M Morel. Landscape evolution models: A review of their fundamen-  
541 tal equations. *Geomorphology*, 219:68–86, 2014.

542 43. D G Tarboton. A new method for the determination of flow directions and upslope areas in  
543 grid digital elevation models. *Water Resources Research*, 33(2):309–319, 1997.

544 44. S Bonetti, D D Richter, and A Porporato. The effect of accelerated soil erosion on hillslope  
545 morphology. *Earth Surface Processes and Landforms*, 2019.

546 45. A Bejan and S Lorente. Design with constructal theory. 2008.

547 46. B B Mandelbrot. *The fractal geometry of nature*, volume 1. WH freeman New York, 1982.

548 47. I Rodríguez-Iturbe, A Rinaldo, R Rigon, R L Bras, E Ijász-Vásquez, and A Marani. Fractal  
549 structures as least energy patterns: The case of river networks. *Geophysical Research*  
550 *Letters*, 19(9):889–892, 1992.

551 48. A Flammini and F Colaiori. Exact analysis of the Peano basin. *Journal of Physics A: Mathe-*  
552 *matical and General*, 29(21):6701, 1996.

553 49. D R Montgomery, G Balco, and S D Willett. Climate, tectonics, and the morphology of the  
554 Andes. *Geology*, 29(7):579–582, 2001.

555 50. L E L Lowman and A P Barros. Investigating links between climate and orography in the  
556 central Andes: Coupling erosion and precipitation using a physical-statistical model. *Journal*  
557 *of Geophysical Research: Earth Surface*, 119(6):1322–1353, 2014.

558 51. J T Perron, J W Kirchner, and W E Dietrich. Formation of evenly spaced ridges and valleys.  
559 *Nature*, 460:502–505, 2009.

560 52. M C Cross and P C Hohenberg. Pattern formation outside of equilibrium. *Reviews of Modern*  
561 *Physics*, 65(3):851, 1993.

562 53. R L Panton. *Incompressible Flow. Third Edition*. John Wiley & Sons, 1984.

563 54. G Willgoose and G Hancock. Revisiting the hypsometric curve as an indicator of form and  
564 process in transport-limited catchment. *Earth Surface Processes and Landforms*, 23(7):611–  
565 623, 1998.

566 55. S Bonetti and A Porporato. On the dynamic smoothing of mountains. *Geophysical Research*  
567 *Letters*, 44(11):5531–5539, 2017.

568 56. P G Debenedetti and F H Stillinger. Supercooled liquids and the glass transition. *Nature*, 410  
569 (6825):259, 2001.

570 57. M Abramowitz and I A Stegun. *Handbook of mathematical functions*. Dover, New York, 1964.

571 58. C G Canuto, M Y Hussaini, A Quarteroni, and T A Zang. *Spectral methods: Fundamentals*  
572 *in single domains*. Springer, Berlin, 2006.

573 59. C Camporeale, C Canuto, and L Ridolfi. A spectral approach for the stability analysis of turbu-  
574 lent open-channel flows over granular beds. *Theoretical and Computational Fluid Dynamics*,  
575 26(1-4):51–80, 2012.

576 60. Giovanni Battista Chirico, Andrew W Western, Rodger B Grayson, and Günter Blöschl. On  
577 the definition of the flow width for calculating specific catchment area patterns from gridded  
578 elevation data. *Hydrological Processes: An International Journal*, 19(13):2539–2556, 2005.

579 61. K E Sweeney, J J Roering, and C Ellis. Experimental evidence for hillslope control of land-  
580 scape scale. *Science*, 349(6243):51–53, 2015.

581 62. B R Munson, D F Young, T H Okiishi, and W W Huebsch. *Fundamentals of fluid mechanics*.  
582 John Wiley & Sons, 1995.

583 63. S. K. Anand, M. Hooshyar, and A. Porporato. Linear layout of multiple flow-direction networks  
584 for landscape-evolution simulations. *arXiv preprint arXiv:1909.03176*, 2019.